Hybrid and Reconfigurable IPT Systems With High-Misalignment Tolerance for Constant-Current and Constant-Voltage Battery Charging

Yang Chen, *Student Member, IEEE*, Bin Yang, Zhihao Kou, Zhengyou He, *Senior Member, IEEE*, Guangzhong Cao, *Member, IEEE*, and Ruikun Mai, *Member, IEEE*

***Abstract*—Inductive power transfer (IPT) for battery charging applications has significant advantages over the traditional plug-in system. Since misalignment between the primary and secondary windings is inevitable, it is of significance to improve the misalignment tolerance of IPT systems with constant-current (CC) and constant-voltage (CV) outputs for battery charging. In this paper, the load-independent output characteristic of the hybrid topology and the function switching between CC and CV of the reconfigurable topology are analyzed. Besides, a hybrid and reconfigurable IPT system with 3-D misalignment tolerance for CC and CV outputs is proposed, simplifying or even canceling control schemes. Moreover, a novel parametric design method is given for the IPT system, which can suppress the fluctuation of the output voltage/current within a certain range of misalignment. In order to validate the performance of the proposed topology, a 1-kW prototype is built, and the corresponding experiments are carried out. In the CC/CV mode, the system can operate with the longitudinal misalignment to 50% when the load varies from 36 to 480 Ω, and the fluctuation of the output current/voltage is within 5%. Similarly, the misalignment in *Y*- and *Z*-axis is 12.5% and 33.3%, respectively.**

***Index Terms*—Battery charging, constant current (CC), constant voltage (CV), high-misalignment tolerance, hybrid and reconfigurable inductive power transfer (IPT) systems.**

I. Introduction

INDUCTIVE power transfer (IPT) technology [1]–[3], based on magnetic coupling, has been adopted in many applications such as consumer electronics [4], biomedical implant devices [5], underwater power supplies [6], electric vehicles (EVs) [7]–[9], train power supplies [10], etc. Compared to conventional plug-in systems, IPT systems are more convenient, flexible, safer, and weatherproof. Some companies, such as ZET, Mgeek, Evatran, WiTricity, etc., have developed many IPT-based products for battery charging. Due to the exploding of EVs in people's daily life, the EV wireless charging may be one of the best solutions to free people from the tiresome plug-in action. However, more research work is still required to reduce control scheme complexity and to increase misalignment tolerance.

Lithium-ion batteries are widely adopted in smartphones and EVs. Typically, the profile of batteries is with the constant-current (CC) mode at first and then the constant-voltage (CV) mode, which aims at prolonging the battery lifetime and recycle time. During the whole charging process, the battery equivalent resistance R_B ($R_B = v_B/i_B$, where v_B and i_B are the charging voltage and charging current, respectively) varies from several ohms up to hundreds of ohms. There are mainly two categories of control schemes for IPT systems operating with CC or CV outputs against variable loads. 1) The control schemes for a high-frequency inverter (HFI): The IPT systems with phase shift control schemes for the HFI can adjust the charging current or charging voltage against various loads [11]. Besides, the systems with load-independent currents/voltages against variable loads can operate at spilt frequencies [12], [13], which may cause a stability issue due to the occurrence of frequency bifurcation phenomenon. 2) The control schemes for dc–dc converters placed on the primary side or the secondary side: The duty cycle of the dc–dc converters can be modulated to achieve desired output currents or output voltages [14], [15]. The IPT systems with aforementioned control schemes can regulate the output currents or voltages with load and coupling variations, but they are at the expense of a wide range of input modulation index and/or complicated control circuitry [16].

Some scholars pay attention to the compensation topologies for CC or CV output replacing the complex control methods. A series of individual passive resonant networks and some higher order compensations for IPT systems CC or CV output are systematically analyzed in [16] and [17]. Besides, some new compensation topologies such as inductor–capacitor–series and series–capacitor–inductor–capacitor topologies for CC and CV

Manuscript received November 16, 2017; revised January 11, 2018; accepted February 22, 2018. Date of publication February 27, 2018; date of current version July 15, 2018. This work was supported in part by the National Science Fund for Distinguished Young Scholars under Grant 51525702, in part by the National Natural Science Foundation of China under Grant 51677155 and Grant 51677120, and in part by the Sichuan Youth Science and Technology Foundation (2016JQ0033). Recommended for publication by Associate Editor C. T. Rim. *(Corresponding author: Ruikun Mai.)*

Y. Chen, B. Yang, Z. Kou, Z. He, and R. Mai are with the School of Electrical Engineering, Southwest Jiaotong University, Chengdu 610031, China (e-mail: yang.chen92@foxmail.com; 546867343@qq.com; 505893546@qq.com; hezy@swjtu.edu.cn; mairk@swjtu.edu.cn).

G. Cao is with the Shenzhen Key Laboratory of Electromagnetic Control, Shenzhen University, Shenzhen 518060, China (e-mail: gzcao@szu.edu.cn).

This paper has supplementary downloadable material available at http://ieeexplore.ieee.org.

Color versions of one or more of the figures in this paper are available online at http://ieeexplore.ieee.org.

Digital Object Identifier 10.1109/TPEL.2018.2809785

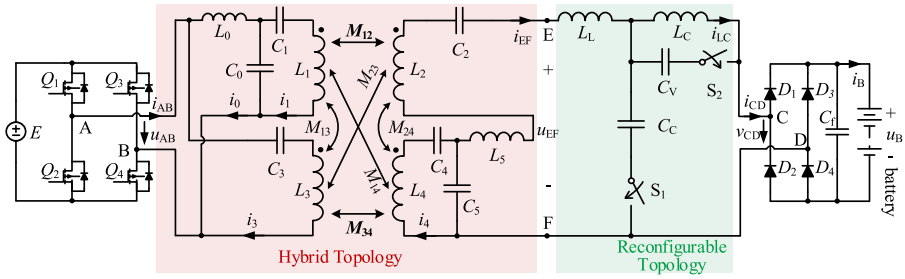

Fig. 1. Hybrid and reconfigurable topology.

outputs are introduced in [18] and [19]. In addition, many efforts are spent in [20]–[22] to combine topologies with CC and CV outputs for battery charging. Four basic topologies including series–series (SS), series–parallel (SP), parallel–parallel, and parallel–series (PS) compensations are discussed in detail, and then, two hybrid topologies are proposed for battery charging [20]. A dual topology switching between SS and SP topologies is given in [21] for CC and CV mode charging. Moreover, a hybrid topology switching between SS and series–inductor–capacitor–capacitor (S-*LCC*) topologies is proposed in work [22], which can charge a fleet of electric bicycles (EBs) with a single inverter. However, all the compensation topologies mentioned above required precise placement of magnetic couplers. Or else, the misalignment leads to system degraded dramatically.

It is essential to improve the misalignment tolerance of IPT systems because the variation of the relative position between the primary and secondary windings is inevitable. The pad misalignments will cause some critical problems such as low power transfer, high power losses, and instability of the systems. Thus, considerable efforts have been made, revolving around coil designs and compensation topologies, to increase the misalignment tolerance of IPT systems. Some authors of the literature [23]–[25] try to optimize the structures of the magnetic couplers to obtain a relatively uniform magnetic field distribution. Additionally, a series–parallel–series topology, which combines the characteristics of SS and PS configurations, is proposed in [26]. The new compensation topology can transfer rated power with high misalignment up to 25% over a 1-D lateral misalignment. In [27], the optimization for compensating capacitor in four-coil coupled wireless charging system can extend the tolerant lateral misalignment up to 44.3%. Multiphase couplers are utilized to increase the vertical and horizontal misalignment tolerances for relatively constant power [28]. In [29], a hybrid bidirectional wireless EV charging system is proposed with 17% vertical misalignment and 41% longitudinal misalignment, maintaining 95% of its nominal power level. Moreover, a dual-side detuned SS compensation topology is used in the IPT system, of which the power transfer varies from 80% to 100% of its nominal power level [30]. All the efforts above do not involve the CC–CV charging research with high misalignment.

A hybrid and reconfigurable IPT system is proposed in this paper to overcome the drawback of misalignment and to provide the characteristics of CC or CV outputs. The hybrid and reconfigurable topology consists of a hybrid topology and a reconfigurable topology, as shown in Fig. 1. The hybrid topology is formed by an inductor-capacitor-capacitor–series (*LCC*-S) topology and an S-*LCC* topology, where the *LCC* represents the inductor–capacitor–capacitor compensation network, and S stands for the capacitor in series with the primary or secondary coil. The two topologies connected in parallel at the primary side aim at decreasing the number of HFIs. The two topologies can also be driven by two HFIs, separately. Since both topologies hold the characteristic of load-independent output voltage, they are chosen to connect in series at the secondary side instead of in parallel. The reconfigurable topology consists of an inductor–capacitor–inductor (*LCL*) topology, two ac switches (ACSs), and an additional capacitor. An ACS in series with the capacitor of *LCL* and the extra capacitor in series with another ACS together connect with the last inductor of *LCL* in parallel.

The contributions of the paper are listed as follows.

1) This paper systematically analyzes the load-independent voltage output, misalignment tolerance characteristics of a hybrid topology formed by LCC-S and S-LCC topologies, and the function switching between CC and CV of the reconfigurable topology. Then, an innovative hybrid and reconfigurable topology is proposed for CC and CV outputs with the ability of suppressing 3-D misalignments, simplifying the control schemes.
2) The misalignment tolerance analysis of double-D quadrature pad (DDQP) is presented in this paper. Then, a novel parametric design method for the hybrid and reconfigurable topology is proposed, so that the fluctuation of the output voltage can be limited within a certain range of misalignment tolerances.

The proposed method has a high misalignment in the *X*-axis but cannot have a high misalignment in the *Y*-axis, so the applications are limited. As for EV or buses, the *y*-misalignment (front-to-rear) may be readily adjusted because the direction of the EV is parallel to the *Y*-axis. In this case, a sensor that informs the current *y*-misalignment to the user is additionally required or can easily be neglected with the help of the user. Additionally, the method can be applied for trams for the reason that the *y*-misalignment hardly exists due to the railway track.

The rest of this paper is organized as follows. The analysis of the hybrid and reconfigurable topology is presented, and the basic characteristics are described in Section II. The misalignment tolerance of two pads and the parametric design method are analyzed in Section III. The hybrid and reconfigurable topology for battery charging is implemented for validation in Section IV. Finally, the conclusion is drawn in Section V.

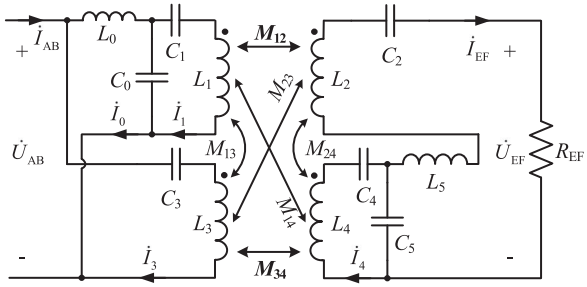

Fig. 2. Hybrid topology driven by a voltage source.

II. Theoretical Analysis

The proposed hybrid and reconfigurable topology is shown in Fig. 1. The HFI has a full bridge consisting of four power MOSFETs (Q_1–Q_4). L_0, C_0, and C_1 (L_5, C_5, and C_4) constitute the *LCC* compensation network, while C_3 (C_2) is part of the S compensation network, together forming *LCC*-S (S-*LCC*) topology. L_L, C_C, and L_C constitute the *LCL* topology, combining C_V and ACSs S_1 and S_2, together forming the reconfigurable topology. The mutual inductances between the four coils are M_{12}, M_{13}, M_{14}, M_{23}, M_{24}, and M_{34}. The rectifier comprises four diodes (D_1–D_4) and a filter capacitor $C_{\rm f}$. Besides, the resonant tank is assumed to be lossless (equivalent series resistance is zero), and semiconductor switches are ideal. The fundamental harmonic approximation method is used to analyze the system.

A. Analysis of the Hybrid Topology

The hybrid and reconfigurable topology is separated intentionally for analyzing, and the hybrid topology is illustrated in Fig. 2. The circuit is driven by a sinusoidal voltage source with angular frequency ω. The topology can be represented by the following equations:

$$\begin{cases} j\omega L_1 + 1/(j\omega C_1) = j\omega L_0 = -1/(j\omega C_0) \\ j\omega L_2 = -1/(j\omega C_2) \\ j\omega L_4 + 1/(j\omega C_4) = j\omega L_5 = -1/(j\omega C_5) \\ j\omega L_3 = -1/(j\omega C_3). \end{cases} \tag{1}$$

According to Kirchhoff's laws, the hybrid circuit can be expressed by

$$\begin{bmatrix} \dot{U}_{\rm AB} \\ 0 \\ 0 \\ \dot{U}_{\rm AB} \\ 0 \end{bmatrix} = \begin{bmatrix} Z_{00} & Z_{01} & Z_{02} & Z_{03} & Z_{04} \\ Z_{10} & Z_{11} & Z_{12} & Z_{13} & Z_{14} \\ Z_{20} & Z_{21} & Z_{22} & Z_{23} & Z_{24} \\ Z_{30} & Z_{31} & Z_{32} & Z_{33} & Z_{34} \\ Z_{40} & Z_{41} & Z_{42} & Z_{43} & Z_{44} \end{bmatrix} \begin{bmatrix} \dot{I}_0 \\ \dot{I}_1 \\ \dot{I}_{EF} \\ \dot{I}_3 \\ \dot{I}_4 \end{bmatrix} \tag{2}$$

where

$$\begin{aligned} &Z_{00} = j\omega L_0 + 1/(j\omega C_0), \quad Z_{01} = Z_{10} = -1/(j\omega C_0) \\ &Z_{02} = Z_{20} = 0, \quad Z_{03} = Z_{30} = 0, \quad Z_{04} = Z_{40} = 0 \\ &Z_{11} = 1/(j\omega C_0) + 1/(j\omega C_1) + j\omega L_1 \\ &Z_{12} = Z_{21} = -j\omega M_{12} \\ &Z_{13} = Z_{31} = j\omega M_{13}, \quad Z_{14} = Z_{41} = -j\omega M_{14} \\ &Z_{22} = j\omega L_2 + 1/(j\omega C_2) + j\omega L_5 + 1/(j\omega C_5) + R_{\rm EF} \\ &Z_{23} = Z_{32} = -j\omega M_{23}, \; Z_{24} = Z_{42} = j\omega M_{24} - 1/(j\omega C_5) \\ &Z_{33} = j\omega L_3 + 1/(j\omega C_3), \quad Z_{34} = Z_{43} = -j\omega M_{34} \\ &Z_{44} = j\omega L_4 + 1/(j\omega C_4) + 1/(j\omega C_5). \end{aligned} \tag{3}$$

By choosing a proper magnetic coupler, the cross couplings (M_{13}, M_{14}, M_{23}, and M_{24}) have much less effects on the output of the system than that of the main couplings (M_{12} and M_{34}) with designed coil structures, which will be discussed in Section III. Therefore, the effects of cross couplings (M_{13}, M_{14}, M_{23}, and M_{24}) are neglected. By solving (2), we can obtain

$$\begin{cases} \dot{I}_0 = \frac{(M_{12}M_{34}+L_0L_5)M_{12}\dot{U}_{\rm AB}}{M_{34}R_{\rm EF}L_0^2} \\ \dot{I}_{\rm EF} = \frac{(M_{12}M_{34}+L_0L_5)\dot{U}_{\rm AB}}{M_{34}R_{\rm EF}L_0} \\ \dot{I}_3 = \frac{(M_{12}M_{34}+L_0L_5)\omega L_5\dot{U}_{\rm AB}}{\omega R_{\rm EF}L_0M_{34}^2}. \end{cases} \tag{4}$$

Then, the voltage gain $G_{\rm VVh}$ of the hybrid topology is given as

$$G_{\rm VVh} = \frac{\dot{I}_{\rm EF}R_{\rm EF}}{\dot{U}_{\rm AB}} = \frac{M_{12}}{L_0} + \frac{L_5}{M_{34}}. \tag{5}$$

It shows that the output voltage of the hybrid topology is load independent by neglecting the cross couplings, which take the advantages of the characteristics of *LCC*-S and S-*LCC* configurations. The role of the *LCC*-S topology is to increase the output voltage with the decrease of mutual inductance. On the contrary, the role of the S-*LCC* topology is to decrease the output voltage with the decrease of mutual inductance. When the pad misalignment takes place, the main coupling M_{12} and M_{34} will decrease, which causes the decrease of M_{12}/L_0 and the increase of L_5/M_{34}. If the parameters are chosen properly, the voltage gain $G_{\rm VVh}$ can maintain relatively constant in a certain range by canceling out the impact of the increase or decrease of M_{12} and M_{34}. Equation (5) is derived under the assumption of no parasitic resistance in the system. It is very intuitive to show the basic output voltage characteristic of the hybrid topology. As we know, the S compensation on the primary side cannot operate without load (mutual inductance is very small, or even close to zero), or the system will break down because of overcurrent on the primary side. Thus, the hybrid topology cannot work without load.

The input current $\dot{I}_{\rm AB}$ is given by

$$\dot{I}_{\rm AB} = \dot{I}_0 + \dot{I}_3 = \frac{\dot{U}_{\rm AB}(M_{12}M_{34}+L_0L_5)^2}{R_{\rm EF}L_0^2M_{34}^2}. \tag{6}$$

The input equivalent impedance $Z_{\rm ABh}$ can be derived by

$$Z_{\rm ABh} = \frac{\dot{U}_{\rm AB}}{\dot{I}_{\rm AB}} = \frac{R_{\rm EF}L_0^2M_{34}^2}{(M_{12}M_{34}+L_0L_5)^2} \tag{7}$$

which is pure resistant indicating that current $i_{\rm AB}$ and voltage $v_{\rm AB}$ can realize zero phase angle (ZPA).

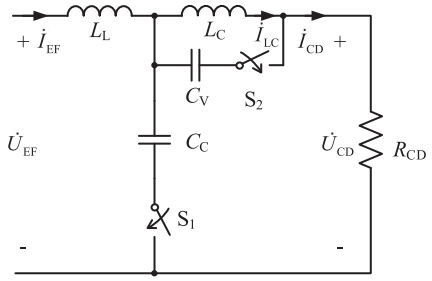

Fig. 3. Reconfigurable topology driven by a voltage source.

B. Analysis of the Reconfigurable Topology

The reconfigurable topology is shown in Fig. 3. When the ACS S_1 is ON and S_2 is OFF, the circuit operating in the CC mode can be described by

$$\begin{bmatrix} \dot{U}_{\rm EF} \\ 0 \end{bmatrix} = \begin{bmatrix} j\omega L_L + \frac{1}{j\omega C_C} & \frac{-1}{j\omega C_C} \\ \frac{-1}{j\omega C_C} & \frac{1}{j\omega C_C} + j\omega L_C + R_{\rm CD} \end{bmatrix} \begin{bmatrix} \dot{I}_{\rm EF} \\ \dot{I}_{\rm CD} \end{bmatrix}. \tag{8}$$

The relationships between inductors L_L and L_C and capacitor C_C are given as follows:

$$\begin{cases} j\omega L_L + \frac{1}{j\omega C_C} = 0 \\ j\omega L_C + \frac{1}{j\omega C_C} = 0. \end{cases} \tag{9}$$

Then, by solving (8), the input and output currents $\dot{I}_{\rm EF}$ and $\dot{I}_{\rm CD}$ are shown as

$$\begin{cases} \dot{I}_{\rm EF} = \dot{U}_{\rm EF} R_{\rm CD} \omega^2 C_C^2 \\ \dot{I}_{\rm CD} = -j\omega C_C \dot{U}_{\rm EF}. \end{cases} \tag{10}$$

Therefore, the current gain $G_{\rm VIr\_CC}$ of the reconfigurable topology in the CC mode is

$$G_{\rm VIr\_CC} = \frac{\dot{I}_{\rm CD}}{\dot{U}_{\rm EF}} = -j\omega C_C. \tag{11}$$

The input equivalent impedance $Z_{\rm EFr\_CC}$ can be derived by

$$Z_{\rm EFr\_CC} = \frac{\dot{U}_{\rm EF}}{\dot{I}_{\rm EF}} = \frac{1}{R_{\rm CD}\omega^2 C_C^2}. \tag{12}$$

When the ACS S_1 is OFF and S_2 is ON, the circuit operates in the CV mode. The relationship of inductors L_L and L_C and capacitor C_V is given by

$$j\omega L_L + \frac{1}{j\omega C_V + 1/(j\omega L_C)} = 0 \tag{13}$$

which indicates that inductors L_L and L_C and capacitor C_V form the series resonance tank. The voltage gain $G_{\rm VVr\_CV}$ of the reconfigurable topology in the CV mode is

$$G_{\rm VVr\_CV} = 1. \tag{14}$$

The input equivalent impedance $Z_{\rm EFr\_CV}$ can be expressed as

$$Z_{\rm EFr\_CV} = R_{\rm CD}. \tag{15}$$

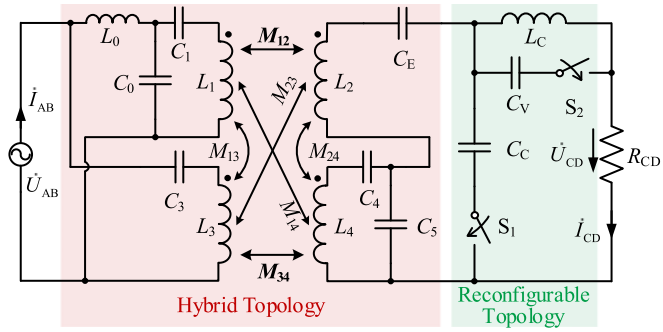

Fig. 4. Combination of the hybrid topology and the reconfigurable topology.

C. Combination of the Hybrid Topology and the Reconfigurable Topology

The hybrid and reconfigurable system is formed by the combination of the hybrid topology and the reconfigurable topology as shown in Fig. 4. Comparing Fig. 1 with Fig. 4, the equivalent impedance of a component noted as C_E (or L_E) is used to replace the equivalent impedance of inductors L_L and L_5 and capacitor C_2. The component C_E (or L_E) can be an inductor L_E or a capacitor C_E, i.e.,

$$j\omega L_L + j\omega L_5 + \frac{1}{j\omega C_2} = j\omega L_E \tag{16}$$

or

$$j\omega L_L + j\omega L_5 + \frac{1}{j\omega C_2} = \frac{1}{j\omega C_E}. \tag{17}$$

The component C_E (or L_E) is treated as a capacitor C_E for simplifying analysis in this section.

CC mode: According to (5) and (11), the current gain $G_{\rm VI}$ of the hybrid and reconfigurable topology is expressed by

$$G_{\rm VI} = G_{\rm VVh} \cdot G_{\rm VIr\_CC} = -j\omega C_C \left(\frac{M_{12}}{L_0} + \frac{L_5}{M_{34}} \right). \tag{18}$$

The corresponding input impedance $Z_{\rm AB\_CC}$ is

$$Z_{\rm AB\_CC} = \frac{L_0^2 M_{34}^2}{R_{\rm CD}\omega^2 C_C^2 (M_{12}M_{34} + L_0 L_5)^2}. \tag{19}$$

CV mode: According to (5) and (14), the voltage gain $G_{\rm VV}$ of the hybrid and reconfigurable topology is obtained

$$G_{\rm VV} = G_{\rm VVh} \cdot G_{\rm VVr\_CV} = \frac{M_{12}}{L_0} + \frac{L_5}{M_{34}}. \tag{20}$$

The corresponding input impedance $Z_{\rm AB\_CV}$ is

$$Z_{\rm AB\_CV} = \frac{R_{\rm CD} L_0^2 M_{34}^2}{(M_{12}M_{34} + L_0 L_5)^2}. \tag{21}$$

It indicates that the input impedance of the hybrid and reconfigurable system in CC and CV modes are both pure resistance, which shows that ZPA can be achieved.

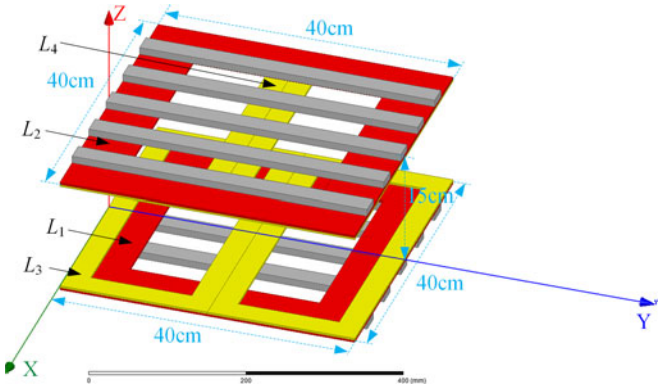

Fig. 5. Structure of DDQP.

III. Parametric Design of the Hybrid and Configurable System

A. Misalignment Tolerance Analysis of DDQP

The magnetic coupler, shown in Fig. 5, is DDQP [31]. The detailed design method of the magnetic coupler is provided in [32]. The misalignment between the pads can be longitudinal (*X*), lateral (*Y*), and vertical (*Z*), which cannot be practically avoided in the charging system. The mutual inductances of a prototype hybrid and reconfigurable IPT system are measured by moving secondary pads longitudinally, laterally, and vertically, separately. The nominal operating point (NOP) of the secondary pads are centered 150 mm directly above the primary pads, where the parameters are designed for high-misalignment tolerance.

The variation in mutual inductances due to the misalignment of secondary pads in *X*-, *Y*-, and *Z*-axis is drawn in Fig. 6. The results indicate that main couplings (M_{12} and M_{34}) have a significant change in *X*- and *Z*-axis, while the cross couplings (M_{13}, M_{14}, M_{23}, and M_{24}) are so small that they can be neglected [32]. To make those cross couplings small like that, the quadrature pad and the double-D pad on the primary or secondary side must be placed in the center of the magnetic coupler in different layers, which means that they are symmetrical. Besides, the DDQPs on the primary side and the secondary side must be symmetrical too. The cross couplings M_{23} and M_{14} are significantly affected by misalignments in the *Y*-axis, so the system cannot have high misalignment in the *Y*-axis with the proposed method.

B. Parametric Design of the Hybrid and Reconfigurable System

Before the parametric design, the values of some parameters should be given first, such as the input dc voltage *E*, the output dc voltage/current U_B/I_B, the mutual inductance M_{34_nop} of the NOP for pads, and the output dc voltage deviation Δ.

The relationship between the input dc voltage *E* and the output ac voltage $U_{\rm AB}$ of the full-bridge HFI can be expressed by [33]

$$U_{\rm AB} = \frac{2\sqrt{2}E}{\pi}. \tag{22}$$

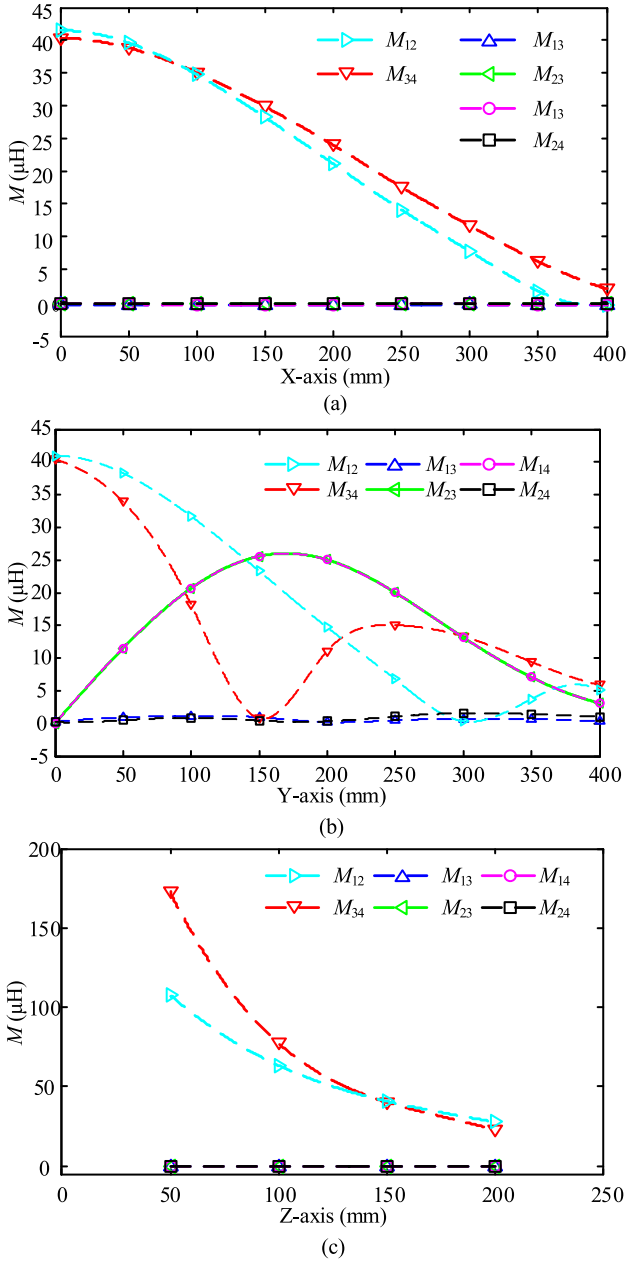

Fig. 6. Variation of mutual inductances due to misalignment of secondary pads in (a) *X*-, (b) *Y*-, and (c) *Z*-axis.

Similarly, the relationship between the input ac voltage/current $U_{\rm CD}/I_{\rm CD}$ and the output dc voltage/current U_B/I_B of the full-bridge diode rectifier can be expressed by [33]

$$\begin{cases} U_B = \frac{\pi\sqrt{2}}{4}U_{\rm CD} \\ I_B = \frac{2\sqrt{2}}{\pi}I_{\rm CD}. \end{cases} \tag{23}$$

As a result, the nominal voltage gain $G_{\rm VVN}$ and the nominal current gain $G_{\rm VIN}$ can be given as

$$\begin{cases} G_{\rm VVN} = \frac{U_{\rm CD}}{U_{\rm AB}} = \frac{U_B}{E} \\ G_{\rm VIN} = \frac{I_{\rm CD}}{U_{\rm AB}} = \frac{\pi^2 I_B}{8E}. \end{cases} \tag{24}$$

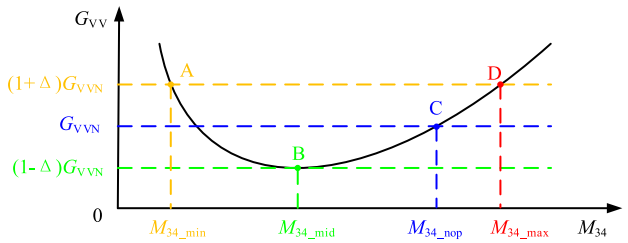

Fig. 7. Relationship between G_{VV} and M_{34}.

The variations of the main couplings M_{12} and M_{34} can be expressed by a function $M_{12} = f(M_{34})$ with the help of MATLAB in a certain range of misalignment. According to Fig. 6(a), the relationship of M_{12} and M_{34} can be approximately a linear model, i.e.,

$$M_{12} = aM_{34} + b. \tag{25}$$

It is not necessary to keep the variations of M_{12} and M_{34} similar. We are concerned about the relationship between M_{12} and M_{34}. In other words, what we need to do is to keep the output voltage $((M_{12}/L_0 + L_5/M_{34})U_{AB})$ varying as small as possible with a certain range of misalignment.

Substituting (25) into (20), we can obtain

$$G_{VV} = \frac{aM_{34} + b}{L_0} + \frac{L_5}{M_{34}}. \tag{26}$$

The relationship between G_{VV} and M_{34} is drawn in Fig. 7, where Δ is the deviation of the output voltage. M_{34_nop} and M_{34_max} are the value at the normal operating point and the maximum value of the misalignment, respectively, and G_{VVN} is the corresponding voltage gain. When the misalignment occurs, M_{34} decreases to M_{34_mid} and the voltage gain decreases to the minimum value $(1-\Delta)G_{VVN}$. Then, M_{34} continues declining until to the minimum value M_{34_min}, and the voltage gain reaches the maximum value $(1+\Delta)G_{VVN}$.

The value of M_{34_mid} can be derived by setting the derivative of G_{VV} to 0, i.e.,

$$\frac{dG_{VV}}{dM_{34}} = 0. \tag{27}$$

By solving (27), we can obtain

$$M_{34\_mid} = \sqrt{\frac{L_0 L_5}{a}}. \tag{28}$$

Substituting point B $(M_{34\_mid}, (1-\Delta)G_{VVN})$ and C (M_{34_nop}, G_{VVN}) into (26), we have

$$\begin{cases} G_{VV}\big|_{M_{34\_mid}} = \frac{aM_{34\_mid}+b}{L_0} + \frac{L_5}{M_{34\_mid}} = (1-\Delta)\,G_{VVN} \\ G_{VV}\big|_{M_{34\_nop}} = \frac{aM_{34\_nop}+b}{L_0} + \frac{L_5}{M_{34\_nop}} = G_{VVN}. \end{cases} \tag{29}$$

The values of L_0 and L_5 can be obtained by solving (29)

$$\begin{cases} L_0 = \frac{A(b+aB)}{G_{VVN}(A+M_{34\_mid}\Delta)} \\ L_5 = \frac{M_{34\_nop}M_{34\_mid}G_{VVN}(aA-b\Delta-M_{34\_nop}a\Delta)}{A(b+aB)} \end{cases} \tag{30}$$

where $A = M_{34\_nop} - M_{34\_mid}$ and $B = M_{34\_nop} + M_{34\_mid}$.

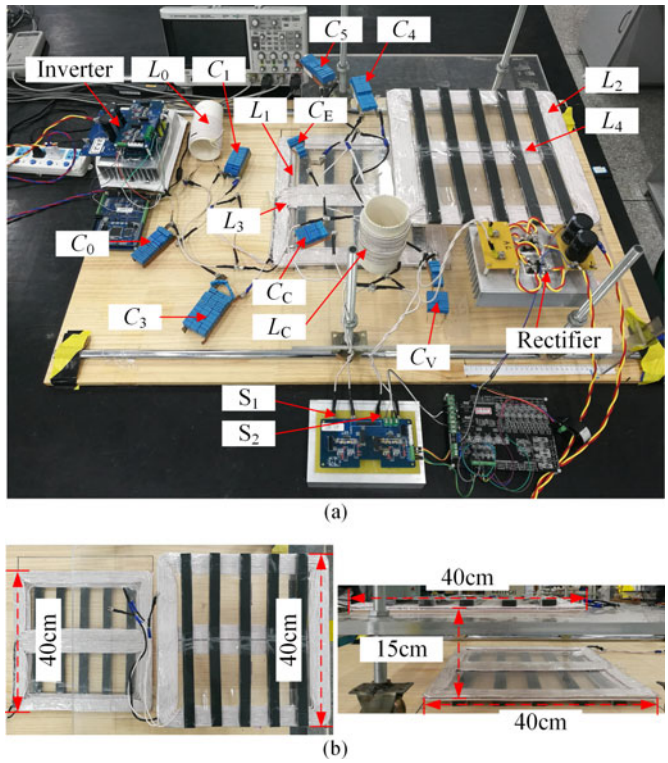

Fig. 8. (a) Setup of the hybrid and reconfigurable IPT system. (b) Structure of coil pads.

According to (18) and (25), we can obtain the value of C_C, i.e.,

$$C_C = G_{VIN} \Big/ \left[\omega\left(\frac{aM_{34\_nop}+b}{L_0} + \frac{L_5}{M_{34\_nop}}\right)\right]. \tag{31}$$

Then, the values of $C_0, C_1, C_2, C_3, C_4, C_5, L_C, L_L, C_V$, and C_E can be calculated according to (1), (9), (13), and (16)/(17).

IV. Experimental Results

In order to demonstrate the applicability of the proposed topology and the above analysis, an experimental prototype of the hybrid and reconfigurable IPT system was designed and built, illustrated in Fig. 8. The switching devices are Q_1–Q_4 = C2M0080120D and S_1 and S_2 = APT56F50L. The system parameters are given in Table I. To simplify the test, an electronic load is used to replace the equivalent load of the batteries in different charging processes.

A. Performance of the IPT System at the NOP

1) Results of Charging an Electronic Load: In the CC mode, the electronic load is changed from 36 to 48 Ω, while in the CV mode, it varies from 48 to 480 Ω. Fig. 9 shows the steady-state waveforms of the output voltage u_{AB}, the output current i_{AB} of the HFI, and the output voltage u_B and output current iB at $R_B = 36\,\Omega$ in the CC mode and at $R_B = 50\,\Omega$ in the CV mode, which indicates that ZPA is achieved, and illustrates that reactive power is eliminated. The transient waveforms of the charging mode from CC to CV are given in Fig. 10. There are

TABLE I
SYSTEM SPECIFICATION AND PARAMETER VALUES

Parameter	Value	Parameter	Value
V_B	220 V	I_B	4.6 A
f	85 kHz	Δ	5%
a	1.188	b	-5.88×10^{-6}
E	110 V	M_{34_nop}	40.1 μH
L_0	32.2 μH	C_0	108.4 nF
C_1	19.1 nF	L_1	217.1 μH
L_2	217.7 μH	C_E	31.6 nF
C_3	15.1 nF	L_3	233.6 μH
L_4	233.7 μH	C_4	17.5 nF
C_5	110.8 nF	C_C	48.7 nF
L_C	71.4 μH	C_V	98.1 nF

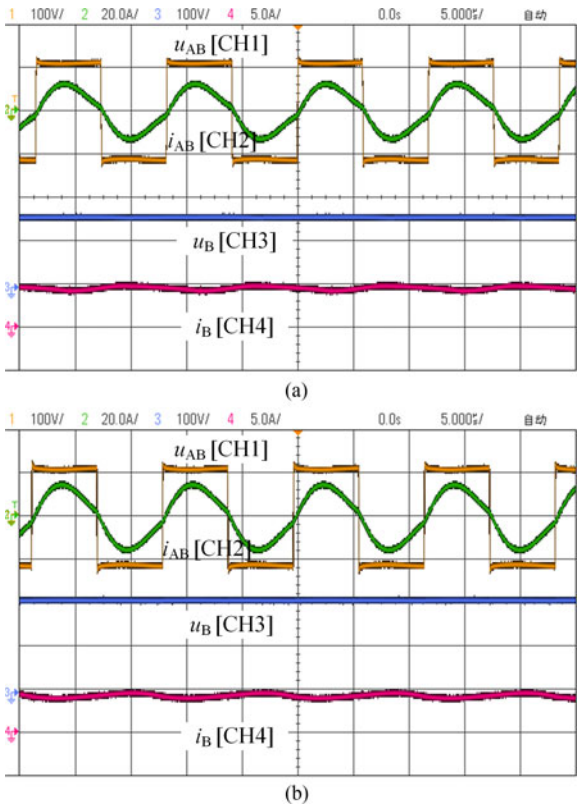

Fig. 9. Experimental waveforms of u_{AB}, i_{AB}, u_B, i_B. (a) $R_B = 36\,\Omega$ in the CC mode. (b) $R_B = 50\,\Omega$ in the CV mode at the NOP.

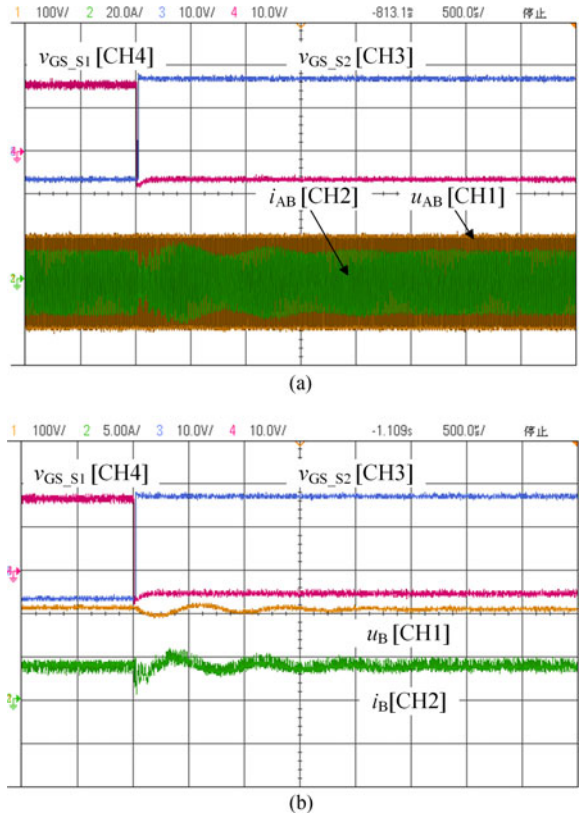

Fig. 10. Transient waveforms from the CC mode to the CV mode of the IPT system. (a) Waveforms of gate drive signals v_{GS_S1} and v_{GS_S2} of ACSs S_1 and S_2, waveforms of i_{AB} and u_{AB}. (b) Waveforms of i_B and u_B.

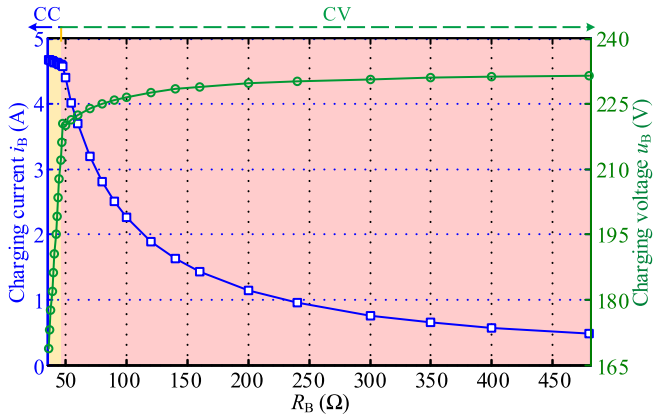

Fig. 11. Measured charging profiles of the hybrid and reconfigurable IPT system versus R_B.

some oscillations during the transient switching mode, and it takes around 2 ms to return to the steady state. The output u_B and i_B nearly remains the same values after mode switching, and the output current i_{AB} of the HFI also maintains relatively invariable. The whole charging profile with the charging current i_B and charging voltage u_B is illustrated in Fig. 11. In the CC mode, the fluctuation of the charging current i_B is less than 5%. In the CV mode, the fluctuation of the charging voltage u_{AB} is within 5%.

A digital power analyzer, PW6001 of HIOKI, is used to measure the input and output dc power, and the efficiency of the IPT system can be obtained. The efficiencies of the hybrid and reconfigurable IPT system are measured as shown in Fig. 12. The efficiency of the IPT system decreases from 92.4% to 91.7% in the CC mode, while in the CV mode, it first climbs from 92.7% to 93.9% and then decreases to 85.7% at the end of the CV mode.

2) Results of Charging a Lead Accumulator: To prove that the simplification of using an electric load is feasible, a lead acid battery is charged in the experiment. Since there is a lead accumulator (4 × 6-DZM-12) with 48-V/12-Ah rating in our laboratory, we regulate the dc input voltage from 110 to 24 V (110–220 V/4.6 A→24–48 V/1 A) to charge the battery. The initial charging voltage of the battery is 44 V, and the charging voltage gradually increases with the charge current of 1 A in the

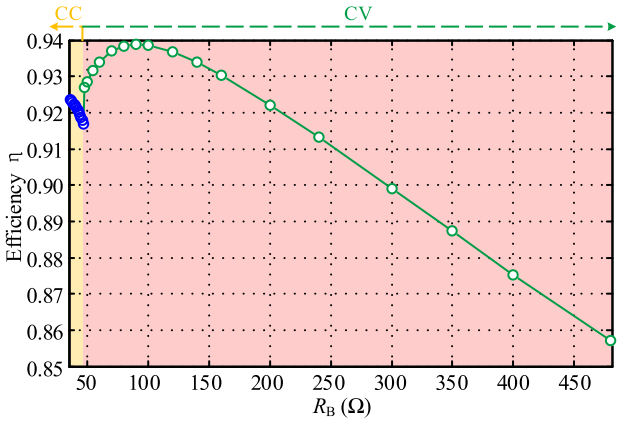

Fig. 12. Measured efficiencies of the hybrid and reconfigurable IPT system in CC and CV modes.

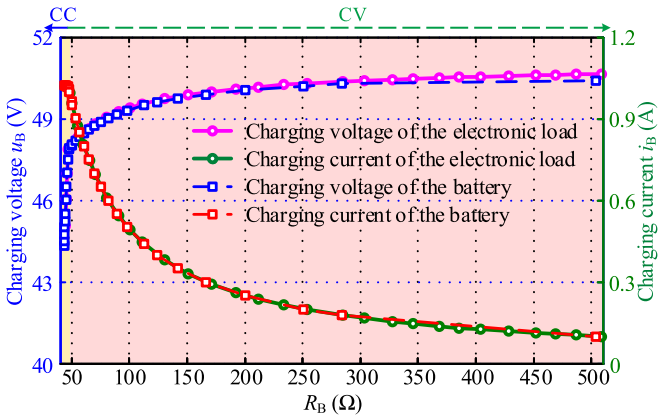

Fig. 13. Measured charging profiles of charging electronic load and battery.

CC mode. When the charging voltage reach 48 V, the charging mode switches from the CC mode to the CV mode. In the CV mode, the charging current decays until it hits the end of charging condition (we set it as 0.1 A in this paper). Both electronic load and lead accumulator are utilized to be charged by the hybrid and reconfigurable IPT system. The measured charging profiles of electronic load and lead accumulator are shown in Fig. 13. The performances indicate that the charging profile of the battery is coincident with that of the electronic load, which means that it is feasible to adopt electric load instead of a battery. Furthermore, the charging current and voltage match the charging profile closely, demonstrating that the proposed method can be used to charge batteries.

The measured efficiencies of charging the battery are illustrated in Fig. 14. The results demonstrate that the efficiencies of the electronic load match that of the lead acid battery very well. During the whole charging process, the efficiency climbs from 91.2% to 92.5% and then decreases to 85.0% with an output power of 5.1 W.

3) Power Loss of ACSs S_1 and S_2: S_1 and S_2 are ACSs, consisting of two antiseries-connected MOSFETs, which is shown in Fig. 15 [22].

ACS S_1 is ON in the circuit for the CC mode, while ACS S_2 is ON for the CV mode. The ACSs only turn ON or turn OFF

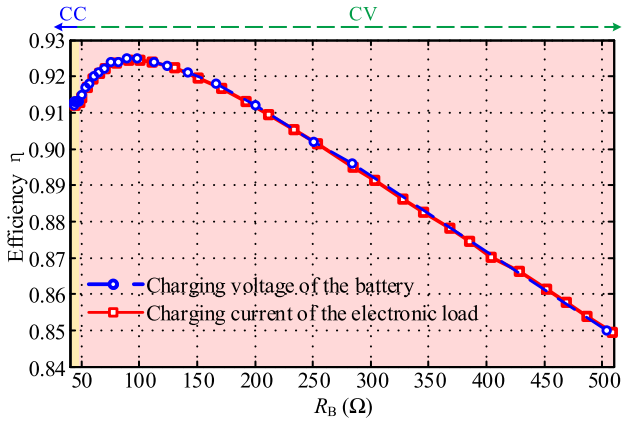

Fig. 14. Measured efficiencies of charging electronic load and battery.

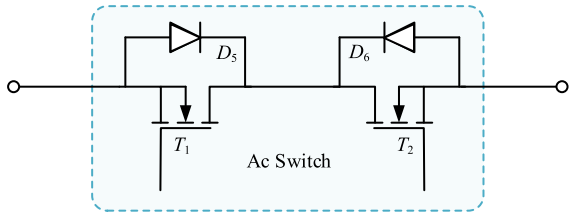

Fig. 15. ACS with two antiseries-connected MOSFETs.

for once. Thus, the switch conduction loss is inevitable, and switching loss can be ignored. The switch conduction loss is determined by the static ON-resistance and the drain current of MOSFET. The semiconductor component's conduction loss P_C is given by [34], [35].

$$P_C = R_{DSon} \times I_{Drms}^2 \tag{32}$$

where R_{DSon} is the drain–source ON-state resistance of MOSFET and I_{Drms} is the RMS value of the MOSFET ON-state current.

In this paper, the ACS is implemented with APT56F50L manufactured by Microsemi. A preliminary assessment of the nominal losses in the ACS has been performed using the information found in the datasheets of the power switches [36]. According to the datasheet of APT56F50L, R_{DSon} is 0.085 Ω. When the IPT system changes the charging mode, the equivalent variable resistance R_B is 48 Ω. At this moment, the current flowing through ACS S_2/S_1 is the maximum. In the CC mode, ACS S_1 is ON and the RMS value of the MOSFET ON-state current I_{Drms_S1} is 7.4 A, and the conduction losses of the two MOSFETs are

$$\begin{aligned} P_{C\_S1} &= 2 \times R_{DSon} \times I_{Drms\_S1}^2 \\ &= 2 \times 0.085 \times 7.4^2 = 9.3 \text{ W}. \end{aligned} \tag{33}$$

In the CV mode, ACS S_2 is ON and the rms value of the MOSFET ON-state current I_{Drms_S2} is 10.2 A, and the conduction loss of the two MOSFETs are

$$\begin{aligned} P_{C\_S2} &= 2 \times R_{DSon} \times I_{Drms\_S2}^2 \\ &= 2 \times 0.085 \times 10.2^2 = 17.7 \text{ W}. \end{aligned} \tag{34}$$

The maximum output power of the IPT system is 1 kW; according to (33) and (34), the switch conduction loss in the CC

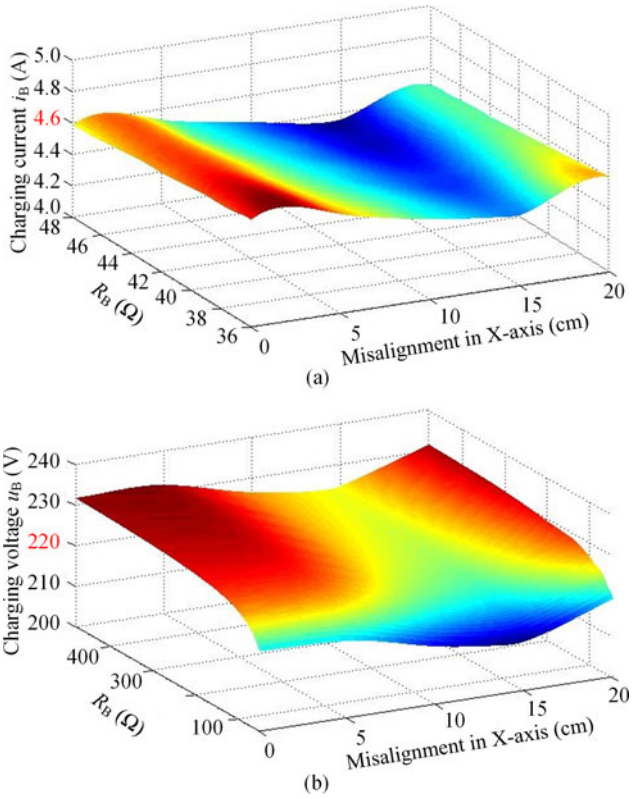

Fig. 16. (a) CC mode: charging current i_B against variable loads with misalignment in the *X*-axis. (b) CV mode: charging voltage u_B against variable loads with misalignment in the *X*-axis.

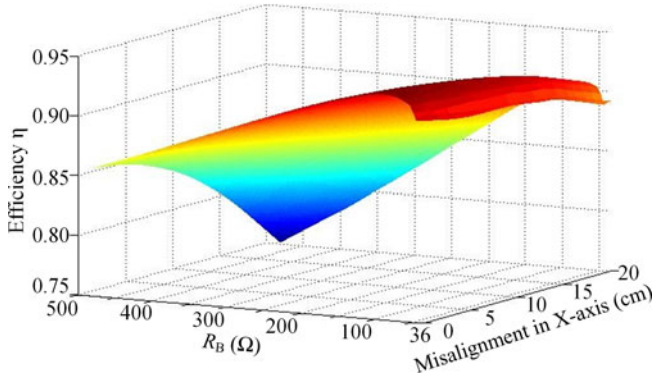

Fig. 17. Measured efficiencies of the IPT system in CC and CV modes with misalignment in the *X*-axis.

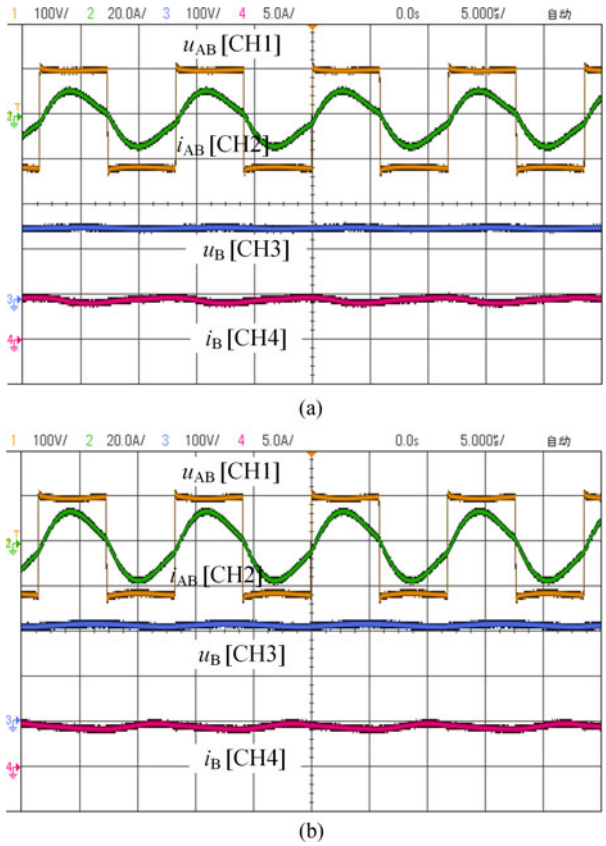

Fig. 18. Experimental waveforms of u_{AB}, i_{AB}, u_B, and i_B. (a) $R_B = 36\,\Omega$ in the CC mode. (b) $R_B = 50\,\Omega$ in the CV mode with the misalignment in the *X*-axis of 20 cm.

mode accounted for 0.9% of the output power, and the switch conduction loss in the CV mode accounted for 1.8% of the output power.

B. Performance of the IPT System With Misalignment

The output current i_B and the output voltage u_B of the IPT system against variable loads with misalignment are shown in Fig. 16. The results demonstrate that the fluctuations of the current i_B and voltage u_B are both within the presupposed deviation Δ, that is 5%. The maximum misalignment in the *X*-axis can achieve 50% with the range of the load from 36 to 480 Ω in CC and CV modes. The efficiencies of the IPT system in CC and CV modes with longitudinal misalignment are shown in Fig. 17. The maximum efficiency is 93.9% at the NOP, and the minimum one is 75.1% with the longitudinal misalignment of 50% at $R_B = 480\,\Omega$. When the misalignment is 20 cm in the *X*-axis, the experimental waveforms of u_{AB} i_{AB}, u_B, and i_B at $R_B = 36\,\Omega$ in the CC mode and at $R_B = 50\,\Omega$ in the CV mode are given in Fig. 18. There is a small phase angle of i_B lagging u_B, which realizes zero-voltage switching of the HFI switches.

Similar experiments with misalignment in *Y*- and *Z*-axis are also observed. As for the misalignment in the *Y*-axis, the designed IPT system only can tolerate the lateral misalignment to 5 cm, i.e., 12.5%. The reason for the smaller misalignment than that in the *X*-axis is that the cross couplings increase much with the misalignment changes. In the *Z*-axis, the IPT system can have the misalignment of ±33.3%, which means that the vertical height of the secondary pads can increase to 200 mm or decrease to 100 mm. The main couplings are both nearly 20 μH ($M_{34\_\min}$) with the height of 200 mm, and they are more than 60 μH ($M_{34\_\max}$) of 100 mm. In this circumstance, the values of the main couplings are not suitable for the proposed parametric design method anymore.

In addition, we measured the currents and voltages of the devices on the secondary side under different charging

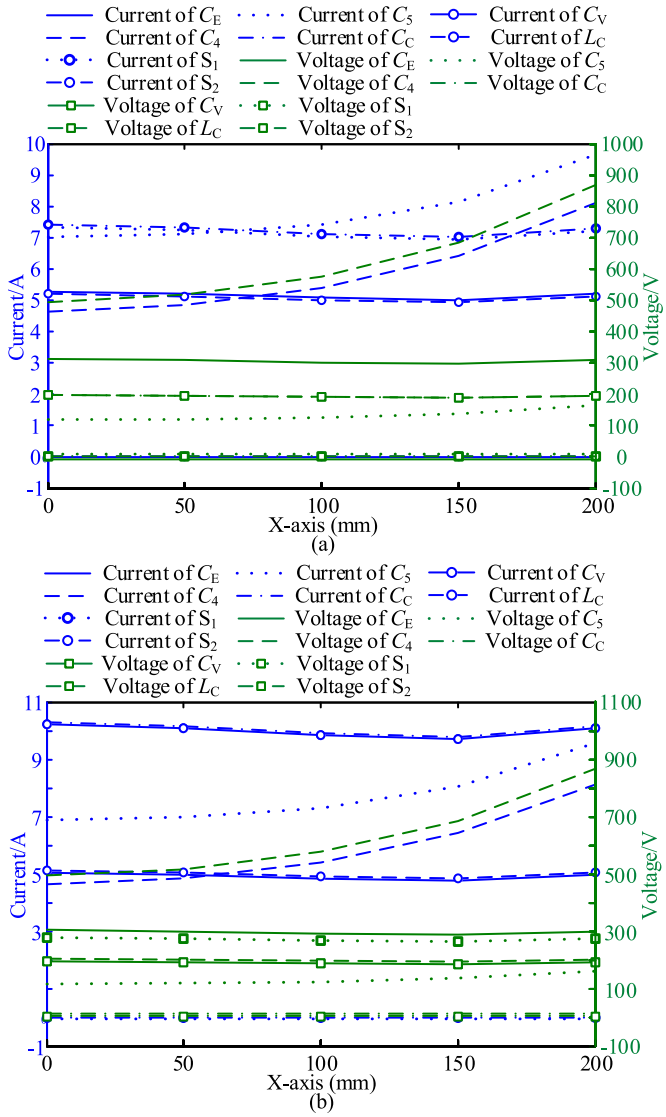

Fig. 19. Measured device stresses on the secondary devices in (a) CC mode and (b) CV mode.

condition (CC and CV modes) and various *x*-misalignments. The measured results are given in Fig. 19. The increase of the misalignment results in the increase of secondary coil current. It indicates that when misalignment happens, the output power of the *LCC*-S topology decreases, while the output power of the S-*LCC* topology increases to keep the output voltage maintaining relatively constant. The performances verify the feasibility of the proposed scheme.

V. Conclusion

An innovative approach for CC and CV outputs with the ability of 3-D misalignments is proposed in this paper. The load-independent output characteristic of the hybrid topology and the function switching between CC and CV of the reconfigurable topology are studied, and the hybrid and reconfigurable topology is proposed, which combines the characteristics of *LCC*-S and S-*LCC* configurations. Moreover, a novel parametric design method for the hybrid and reconfigurable topology is proposed, which can limit the fluctuation of the output voltage/current within a certain range of misalignment tolerances. A 1-kW laboratory-scale prototype having the hybrid and reconfigurable topology has been developed. In the CC/CV mode, the system can operate with the longitudinal misalignment to 50% when the load varies from 36 to 480 Ω, and the fluctuation of the output current/voltage is within 5%. Similarly, the misalignment in *Y*- and *Z*-axis is 12.5% and 33.3%, respectively. The results validate the theoretical analysis and demonstrate the good behavior of the proposed method.

Our future work is about 1) the coupling pads, of which the main couplings vary relatively similar with misalignment in *X*- and *Y*-axis, and 2) the optimization of the variations of the main mutual inductances to increase the misalignment tolerance for the hybrid and reconfigurable IPT system.

References

[1] S. Zhou and C. Chris Mi, "Multi-Paralleled LCC reactive power compensation networks and their tuning method for electric vehicle dynamic wireless charging," *IEEE Trans. Ind. Electron.*, vol. 63, no. 10, pp. 6546–6556, Oct. 2016.

[2] S. Lee, B. Choi, and C. T. Rim, "Dynamics characterization of the inductive power transfer system for online electric vehicles by Laplace phasor transform," *IEEE Trans. Power Electron.*, vol. 28, no. 12, pp. 5902–5909, Dec. 2013.

[3] J. T. Boys, G. A. Covic, and G. A. J. Elliott, "Pick-up transformer for ICPT applications," *Electron. Lett.*, vol. 38, no. 21, pp. 1276–1278, Oct. 10, 2002.

[4] S. Y. Hui, "Planar wireless charging technology for portable electronic products and Qi," *Proc. IEEE*, vol. 101, no. 6, pp. 1290–1301, Jun. 2013.

[5] A. K. RamRakhyani, S. Mirabbasi, and C. Mu, "Design and optimization of resonance-based efficient wireless power delivery systems for biomedical implants," *IEEE Trans. Biomed. Circuits Syst.*, vol. 5, no. 1, pp. 48–63, Feb. 2011.

[6] H. Fukuda *et al.*, "New concept of an electromagnetic usage for contactless communication and power transmission in the ocean," in *Proc. IEEE Int. Underwater Technol. Symp.*, Tokyo, Japan, 2013, pp. 1–4.

[7] W. Y. Lee, J. Huh, and S. Y. Choi, "Finite-width magnetic mirror models of mono and dual coils for wireless electric vehicles," *IEEE Trans. Power Electron.*, vol. 28, no. 13, pp. 1413–1428, Mar. 2013

[8] W. Li, H. Zhao, S. Li, J. Deng, T. Kan, and C. C. Mi, "Integrated LCC compensation topology for wireless charger in electric and plug-in electric vehicles," *IEEE Trans. Ind. Electron.*, vol. 62, no. 7, pp. 4215–4225, Jul. 2015.

[9] D. H. Tran, V. B. Vu, and W. Choi, "Design of a high-efficiency wireless power transfer system with intermediate coils for the on-board chargers of electric vehicles," *IEEE Trans. Power Electron.*, vol. 33, no. 1, pp. 175–187, Jan. 2018.

[10] J. H. Kim *et al.*, "Development of 1-MW inductive power transfer system for a high-speed train," *IEEE Trans. Ind. Electron.*, vol. 62, no. 10, pp. 6242–6250, Oct. 2015.

[11] A. Berger, M. Agostinelli, S. Vesti, J. A. Oliver, J. A. Cobos, and M. Huemer, "A wireless charging system applying phase-shift and amplitude control to maximize efficiency and extractable power," *IEEE Trans. Power Electron.*, vol. 30, no. 11, pp. 6338–6348, Nov. 2015.

[12] D. Ahn and S. Hong, "Wireless power transmission with self-regulated output voltage for biomedical implant," *IEEE Trans. Ind. Electron.*, vol. 61, no. 5, pp. 2225–2235, May 2014.

[13] N. Liu and T. G. Habetler, "Design of a universal inductive charger for multiple electric vehicle models," *IEEE Trans. Power Electron.*, vol. 30, no. 11, pp. 6378–6390, Nov. 2015.

[14] H. H. Wu, G. Aaron, D. S. Kylee, and B. Daniel, "A high efficiency 5 kW inductive charger for EVs using dual side control," *IEEE Trans. Ind. Informat.*, vol. 8, no. 3, pp. 585–595, Aug. 2012.

[15] Z. Li, C. Zhu, J. Jiang, K. Song, and G. Wei, "A 3-kW wireless power transfer system for sightseeing car supercapacitor charge," *IEEE Trans. Power Electron.*, vol. 32, no. 5, pp. 3301–3316, May 2017.

[16] X. Qu, Y. Jing, H. Han, S. C. Wong, and C. K. Tse, "Higher order compensation for inductive-power-transfer converters with constant-voltage or constant-current output combating transformer parameter constraints," *IEEE Trans. Power Electron.*, vol. 32, no. 1, pp. 394–405, Jan. 2017.

[17] W. Zhang and C. C. Mi, "Compensation topologies of high-power wireless power transfer systems," *IEEE Trans. Veh. Technol.*, vol. 65, no. 6, pp. 4768–4778, Jun. 2016.

[18] Y. Wang, Y. Yao, X. Liu, D. G. Xu, and L. Cai, "An LC/S compensation topology and coil design technique for wireless power transfer," *IEEE Trans. Power Electron.*, vol. 33, no. 3, pp. 2007–2025, Mar. 2018, doi: 10.1109/TPEL.2017.2698002.

[19] Y. Wang, Y. Yao, X. Liu, and D. Xu, "S/CLC compensation topology analysis and circular coil design for wireless power transfer," *IEEE Trans. Transp. Electrific.*, vol. 3, no. 2, pp. 496–507, Jun. 2017.

[20] X. Qu, H. Han, S. C. Wong, C. K. Tse, and W. Chen, "Hybrid IPT topologies with constant current or constant voltage output for battery charging applications," *IEEE Trans. Power Electron.*, vol. 30, no. 11, pp. 6329–6337, Nov. 2015.

[21] C. Auvigne, P. Germano, D. Ladas, and Y. Perriard, "A dual-topology ICPT applied to an electric vehicle battery charger," in *Proc. Int. Conf. Elect. Mach.*, Mar. 2012, pp. 2287–2292.

[22] R. Mai, Y. Chen, Y. Li, Y. Zhang, G. Cao, and Z. He, "Inductive power transfer for massive electric bicycles charging based on hybrid topology switching with a single inverter," *IEEE Trans. Power Electron.*, vol. 32, no. 8, pp. 5897–5906, Aug. 2017.

[23] M. Budhia, J. T. Boys, G. A. Covic, and C.-Y. Huang, "Development of a single-sided flux magnetic coupler for electric vehicle IPT charging systems," *IEEE Trans. Ind. Electron.*, vol. 60, no. 1, pp. 318–328, Jan. 2013.

[24] S. Kim, A. Tejeda, G. A. Covic, and J. T. Boys, "Analysis of mutually decoupled primary coils for IPT systems for EV charging," in *Proc. IEEE Energy Convers. Congr. Expo.*, 2016, pp. 1–6.

[25] K. Kalwar *et al.*, "Coil design for high misalignment tolerant inductive power transfer system for EV charging," *Energies*, vol. 9, no. 11, Nov. 2016, Art. no. 937.

[26] J. L. Villa, J. Sallan, J. F. S. Osorio, and A. Llombart, "High-misalignment tolerant compensation topology for ICPT systems," *IEEE Trans. Ind. Electron.*, vol. 59, no. 2, pp. 945–951, Feb. 2012.

[27] Q. Zhu, Y. Guo, L. Wang, C. Liao, and F. Li, "Improving the misalignment tolerance of wireless charging system by optimizing the compensate capacitor," *IEEE Trans. Ind. Electron.*, vol. 62, no. 8, pp. 4832–4836, Aug. 2015.

[28] S. Raabe and G. A. Covic, "Practical design considerations for contactless power transfer quadrature Pick-Ups," *IEEE Trans. Ind. Electron.*, vol. 60, no. 1, pp. 400–409, Jan. 2013.

[29] L. Zhao, D. J. Thrimawithana, and U. K. Madawala, "Hybrid bidirectional wireless EV charging system tolerant to pad misalignment," *IEEE Trans. Ind. Electron.*, vol. 64, no. 9, pp. 7079–7086, Sep. 2017.

[30] H. Feng, T. Cai, S. Duan, X. Zhang, H. Hu, and J. Niu, "A dual-side-detuned series–series compensated resonant converter for wide charging region in a wireless power transfer system," *IEEE Trans. Ind. Electron.*, vol. 65, no. 3, pp. 2177–2188, Mar. 2018.

[31] M. Budhia, J. T. Boys, G. A. Covic, and C. Y. Huang, "Development of a single-sided flux magnetic coupler for electric vehicle IPT charging systems," *IEEE Trans. Ind. Electron.*, vol. 60, no. 1, pp. 318–328, Jan. 2013.

[32] Y. Li, T. Lin, R. Mai, L. Huang, and Z. He, "Compact double-sided decoupled coils based WPT systems for high power applications: Analysis, design and experimental verification," *IEEE Trans. Transp. Electrific.*, vol. 4, no. 1, pp. 64–75, Mar. 2018, doi: 10.1109/TTE.2017.2745681.

[33] R. W. Erickson and D. Maksimovic, *Fundamentals of Power Electronics*, 2nd ed. Norwell, MA, USA: Kluwer, 2001.

[34] K. Colak, E. Asa, M. Bojarski, D. Czarkowski, and O. C. Onar, "A novel phase-shift control of semibridgeless active rectifier for wireless power transfer," *IEEE Trans. Power Electron.*, vol. 30, no. 11, pp. 6288–6297, Nov. 2015.

[35] Y. Attia and M. Youssef, "GaN on silicon E-HEMT and pure silicon MOSFET in high frequency switching of EV DC/DC converter: A comparative study in a Nissan leaf," in *Proc. IEEE Int. Telecommun. Energy Conf.*, Austin, TX, USA, 2016, pp. 1–6.

[36] D. Graovac, M. Pürschel, and A. Kiep, *MOSFET Power Losses Calculation Using the Data-Sheet Parameters*. Neubiberg, Germany: Infineon, 2006. [Online]. Available: http://www.scribd.com/doc/34308439/MOSFET-Power-Losses-Calculation-Using-the-Data-Sheet-Parameters

Yang Chen (S'17) received the B.Sc. degree in electrical engineering and automation from the School of Electrical Engineering, Southwest Jiaotong University, Chengdu, China, in 2015, where he is currently working toward the Ph.D. degree.

His main research interest focuses on wireless power transfer.

Bin Yang received the B.Sc. degree in electrical engineering and automation from the School of Electrical and Automation Engineering, East China Jiaotong University, Nanchang, China, in 2017. He is currently working toward the M.Sc. degree at the School of Electrical Engineering, Southwest Jiaotong University, Chengdu, China.

His main research interest focuses on wireless power transfer.

Zhihao Kou received the B.Sc. degree in bioinformatics from the School of Life Science and Engineering, Southwest Jiaotong University, Chengdu, China, in 2016, where he is currently working toward the M.Sc. degree at the School of Electrical Engineering.

His main research interest focuses on wireless power transfer.

Zhengyou He (M'10–SM'13) received the B.Sc. and M.Sc. degrees in computational mechanics from Chongqing University, Chongqing, China, in 1992 and 1995, respectively, and the Ph.D. degree in power system and automation from the School of Electrical Engineering, Southwest Jiaotong University, Chengdu, China, in 2001.

He is currently a Professor at the School of Electrical Engineering, Southwest Jiaotong University. His research interests include signal process and information theory applied to electrical power systems and applications of wavelet transforms in power systems.

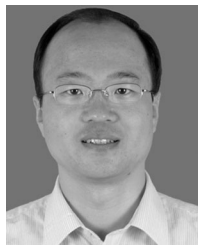

Guangzhong Cao (M'15) received the B.Sc., M.Sc., and Ph.D. degrees in electrical engineering and automation from Xi'an Jiaotong University, Xi'an, China, in 1989, 1992, and 1996, respectively.

He is currently a Professor and Director with the Shenzhen Key Laboratory of Electromagnetic Control, Shenzhen University, Shenzhen, China. He has authored more than 90 articles in refereed journals and conferences. His research interests include motor control and control theory and its application.

Ruikun Mai (M'14) received the B.Sc. degree in electronic and information engineering and the Ph.D. degree in power system and automation from Southwest Jiaotong University, Chengdu, China, in 2004 and 2010, respectively.

He is currently a Professor at the School of Electrical Engineering, Southwest Jiaotong University. His research interests include wireless power transfer and its application in railway systems, power system stability, and control.